Communication

A Stability Extensible Symplectic FDTD$^{(4,4)}$ Method and Its Application in Subgrid Technique for Arbitrary Grid Ratios

Guoda Xie, Naixing Feng, Ming Fang, Mei Song Tong, Wei E. I. Sha, and Zhixiang Huang

***Abstract*— This communication presents a novel algorithm, namely, the 3-D stability extensible spatial-filtering symplectic finite-difference time-domain method (SF-SFDTD$^{(4,4)}$) algorithm, as an enhancement to the traditional finite-difference time-domain (FDTD$^{(2,2)}$) method. The symplectic FDTD$^{(4,4)}$ method, which exhibits higher-order numerical accuracy in both temporal and spatial domains, is utilized as the basis for this algorithm. The primary objective of this research is to overcome the limitations imposed by the Courant–Friedrich–Levy (CFL) condition. To achieve this, the study leverages the SF technique to establish an enlarged CFL condition within the proposed SF-SFDTD$^{(4,4)}$ algorithm. Additionally, a novel hybrid subgrid technique is introduced to accommodate arbitrary coarse/dense grid ratios within the simulation domain. Specifically, the standard FDTD$^{(2,2)}$ method is employed in the coarse grid region, while the proposed SF-SFDTD$^{(4,4)}$ method is applied to the dense grid region. This approach ensures that the entire simulation can employ the same time increment determined by the stability condition of the coarse grid, owing to the highly stable characteristic of the SF-SFDTD$^{(4,4)}$ method. To confirm the accuracy and advantages of the proposed SF-SFDTD$^{(4,4)}$ algorithm and its extended method of hybrid subgrid technique, some numerical examples are carried out. The results demonstrate the efficacy of the algorithm in terms of both efficiency and memory requirement.**

***Index Terms*— Spatial filtering (SF), subgrid technique, symplectic finite-difference time-domain method (SFDTD).**

I. Introduction

Successful applications of the finite-difference time-domain (FDTD) method has demonstrated their strength in terms of scalability and versatility [1], [2]. Nevertheless, this method exhibits certain deficits, including 2nd-order accuracies in both temporal and spatial domains, as well as an explicit characteristic that limits the maximum temporal increment and leads to inefficiencies. To address these limitations, an effective scheme is proposed based on high-order (HO) accuracy to mitigate numerical dispersion. Initially, the HO-FDTD$^{(4,4)}$ algorithm is introduced, which achieves 4th-order accuracy in both spatial and temporal domains [3]. By adopting lower mesh resolution and larger time increments, the efficiency and memory consumption of the HO-FDTD algorithm can be reduced. Additionally, the symplectic FDTD$^{(4,4)}$ [symplectic finite-difference time-domain method (SFDTD$^{(4,4)}$)] method is presented, which combines the 4th-order accuracy in the spatial domain with the application of a multisymplectic integrator propagator in the temporal domain [4], [5]. The SFDTD$^{(4,4)}$ method offers an accurate and stable solution for long-term simulations compared to the standard FDTD$^{(2,2)}$ algorithm. This is due to its energy-conserving characteristics and preservation of the phase space volume of the Hamiltonian system. However, the stability condition of the SFDTD$^{(4,4)}$ algorithm is still subject to the constraints of the Courant–Friedrich–Levy (CFL) condition. Therefore, the calculation efficiency is reduced when using a small time step increment in the SFDTD$^{(4,4)}$ method. Therefore, it is crucial to develop a highly stable SFDTD$^{(4,4)}$ approach while maintaining high accuracy to facilitate its application in numerical calculations. Additionally, applying the SFDTD$^{(4,4)}$ method to subgrid technique further enhances the calculation advantages of the proposed highly stable SFDTD$^{(4,4)}$ method in electromagnetic (EM) simulations.

In this communication, a highly stable 3-D spatial filtering SFDTD$^{(4,4)}$ (SF-SFDTD$^{(4,4)}$) method is proposed. The method effectively addresses the CFL limitation observed in the standard SFDTD$^{(4,4)}$ approach by leveraging SF techniques as previously discussed in references [6] and [7]. Importantly, our proposed method does not require a complete reformulation of the standard SFDTD$^{(4,4)}$ method, making it more practical for implementation. The SF-SFDTD$^{(4,4)}$ method shares similar updating formulas for field components with the standard SFDTD$^{(4,4)}$ approach. However, it incorporates an SF procedure in each iteration, making it easier to implement in practical applications. The study performed numerical experiments with the SF-SFDTD$^{(4,4)}$ method to verify its accuracy and efficiency when compared to the standard SFDTD$^{(4,4)}$ method. Additionally, the study introduces a subgrid scheme that combines the proposed SF-SFDTD$^{(4,4)}$ method with the conventional FDTD$^{(2,2)}$ method. The SF-SFDTD$^{(4,4)}$ method is employed in the dense grid region, while the FDTD$^{(2,2)}$ method is used in the coarse grid region. To ensure overall stability, the temporal increment is determined based on the stability condition of the coarse grid. Notably, the SF operations expand the stability condition of the SF-SFDTD$^{(4,4)}$ method, eliminating the need for timing synchronization between coarse and dense regions. Additionally, a more versatile hybrid subgrid technique is introduced which allows arbitrary configuration of proportions between coarse- and dense-grid generation, thereby enhancing its generality. The advantages of the proposed hybrid subgrid method are confirmed through the simulation of a 3-D EM structure with inhomogeneous and dispersive media.

The communication is structured as follows. Section II presents the SF theory for the 3-D SFDTD$^{(4,4)}$ method. This section includes the derivation processes for extending the CFL limitation of the standard

Manuscript received 2 August 2022; revised 24 June 2023; accepted 21 July 2023. Date of publication 18 August 2023; date of current version 30 October 2023. This work was supported in part by the National Nature Science Foundation of China under Grant 62201003, Grant 62271004, Grant 62231003, Grant U20A20164, and Grant 62301001; and in part by the Anhui Province Key Research and Development Plane under Grant 2023z04020018. *(Corresponding author: Ming Fang.)*

Guoda Xie, Naixing Feng, Ming Fang, and Zhixiang Huang are with the Key Laboratory of Intelligent Computing and Signal Processing, Ministry of Education, the Information Materials and Intelligent Sensing Laboratory of Anhui Province, and the Key Laboratory of Electromagnetic Environmental Sensing of Anhui Higher Education Institutes, Anhui University, Hefei 230601, China (e-mail: mingfang@ahu.edu.cn).

Mei Song Tong is with the Key Laboratory of Embedded System and Service Computing of the Ministry of Education, College of Electronics and Information Engineering, Tongji University, Shanghai 200092, China.

Wei E. I. Sha is with the Key Laboratory of Micro-Nano Electronic Devices and Smart Systems of Zhejiang Province, College of Information Science and Electronic Engineering, Zhejiang University, Hangzhou 310027, China.

Color versions of one or more figures in this communication are available at https://doi.org/10.1109/TAP.2023.3304984.

Digital Object Identifier 10.1109/TAP.2023.3304984

SFDTD$^{(4,4)}$ method, the numerical dispersion analysis of the proposed method, and the technique of combining the SF-SFDTD$^{(4,4)}$ method with the FDTD$^{(2,2)}$ method to develop the subgrid technique. In Section III, several numerical models are simulated to demonstrate the accuracies and efficiencies of the proposed SF-FDTD$^{(4,4)}$ method and the hybrid subgrid SF-SFDTD$^{(4,4)}$ method. Finally, the communication discusses and draws the conclusions.

II. SF Theory For SFDTD$^{(4,4)}$ Method

A. Extending the Stability Limitation of the 3-D SFDTD$^{(4,4)}$ Method

For the standard 3-D SFDTD$^{(4,4)}$ approach, the CFL limitation is derived from the following equation introduced in [4]:

$$|\zeta| \le 1 \tag{1}$$

where

$$\zeta \le 1 + \frac{1}{2}\sum_{l=1}^{m} g_l \left\{ c_0^2 \Delta t^2 \left(\eta_x^2 + \eta_y^2 + \eta_z^2 \right) \right\}^l \tag{2}$$

$$g_l = \sum_{\substack{1\le i_1\le j_1<i_2\le j_2 \\ <\cdots<i_l\le j_l\le m}} c_{i_1} d_{j_1} c_{i_2} d_{j_2}, \ldots, c_{i_l} d_{j_l} + \sum_{\substack{1\le i_1< j_1\le i_2< j_2 \\ \le\cdots\le i_l< j_l\le m}} c_{i_1} d_{j_1} c_{i_2} d_{j_2}, \ldots, c_{i_l} d_{j_l} \tag{3}$$

$$\begin{aligned} &\eta_x^2 + \eta_y^2 + \eta_z^2 \\ &= -4 \times \left\{ \left(\frac{1}{\Delta x} \right)^2 \left[\frac{9}{8} \sin\left(\frac{k_x \Delta x}{2} \right) - \frac{1}{24} \sin\left(\frac{3k_x \Delta x}{2} \right) \right]^2 \right. \\ &\quad + \left(\frac{1}{\Delta y} \right)^2 \left[\frac{9}{8} \sin\left(\frac{k_y \Delta y}{2} \right) - \frac{1}{24} \sin\left(\frac{3k_y \Delta y}{2} \right) \right]^2 \\ &\quad \left. + \left(\frac{1}{\Delta z} \right)^2 \left[\frac{9}{8} \sin\left(\frac{k_z \Delta z}{2} \right) - \frac{1}{24} \sin\left(\frac{3k_z \Delta z}{2} \right) \right]^2 \right\}. \end{aligned} \tag{4}$$

The value of g_l could be calculated via the symplectic integration coefficients c_l and d_l; m denotes the sub-time steps in each iteration. Let

$$\mathrm{Q} = -(\Delta/2)^2 \left(\eta_x^2 + \eta_y^2 + \eta_z^2 \right). \tag{5}$$

Then according to (1) and (2), the inequality for the time step used in standard SFDTD$^{(4,4)}$ method is derived as

$$\Delta t \le (\Delta/c_0) \times (3.003/2) \times (1/\sqrt{\mathrm{Q}}). \tag{6}$$

To ensure stability, Δt must be smaller than the upper limit of the right hand of (6). Considering the condition $\sin(k_s \Delta s/2) = 1$, $\sin(3k_s \Delta s/2) = -1 (s = x, y, z)$ ensures a real wavenumber. Therefore, it is assumed that $\Delta x = \Delta y = \Delta z = \Delta$ and $\sin(k_s \Delta s/2) = 1$, $\sin(3k_s \Delta s/2) = -1 (s = x, y, z)$. Next, the CFL limitation of the standard SFDTD$^{(4,4)}$ can be obtained from (6)

$$\Delta t_{\mathrm{CFL}} \le 0.7431 \times \Delta/c_0. \tag{7}$$

The CFL limitation of the standard SFDTD$^{(4,4)}$ method in (7) ensures that all spatial-frequency components remain stable, which is the primary constraint of the time-step size. In effect, the excited signal only engages a small part of the bandwidth. The remaining part of the bandwidth contains no signal information, but increases the numerical dispersion which constrains the time step size for stable computations. For instance, to improve the numerical accuracy, the grid size Δ is usually less than $\lambda_{\min}/10$. If $\Delta = \lambda_{\min}/10$, then the highest wavenumber of the excited signal is

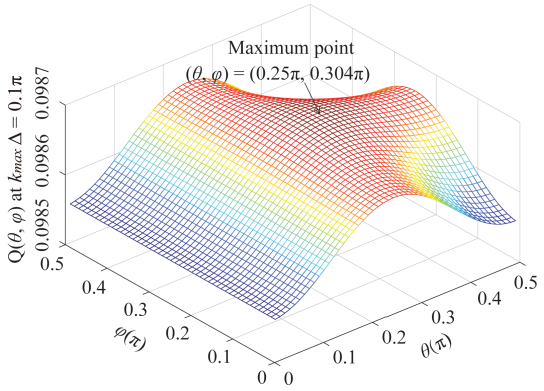

Fig. 1. Value of $Q(\theta, \phi)$ versus θ and ϕ with $k_{\max}\Delta = 0.1\pi$.

$k_{\text{highest}} = 2\pi/\lambda_{\min} = \pi/(5\Delta)$ [8]. However, according to the Nyquist sampling theory, $f_{\max} = 1/(2\Delta)$ is the maximum spatial frequency in the SFDTD$^{(4,4)}$ calculation, thus the wavenumber $k_0 = 2\pi/\lambda_{\min} = 2\pi f_{\max} = 2\pi/(2\Delta) = \pi/\Delta$ is the greatest wavenumber that the SFDTD$^{(4,4)}$ can accommodate. Therefore, the wavenumber from $\pi/(5\Delta)$ to π/Δ does not carry source excitation but generate undesired dispersion errors. Fortunately, these spurious frequency components can be filtered out and almost do not influence the accuracy of the numerical method. For example, assuming that the available wavenumbers k in each direction are located at a radius $k_{\max}$ ($k \le k_{\max}$) [6], [7], $k_{\max}$ is the filtering wavenumber, and the spatial frequency components beyond $k_{\max}$ and π/Δ is filtered out, the numerical wavenumber k is defined as

$$(k_x, k_y, k_z) = (k_{\max} \sin\theta \cos\varphi, k_{\max} \sin\theta \sin\varphi, k_{\max} \cos\theta) \tag{8}$$

where θ and ϕ are the propagation angles, substituting (8) into (5), then we have

$$\begin{aligned} &\mathrm{Q}(\theta, \varphi) \\ &= \left\{ \left[\frac{9}{8} \sin\left(\frac{k_{\max}\Delta}{2} \sin\theta \cos\varphi \right) - \frac{1}{24} \sin\left(\frac{3k_{\max}\Delta}{2} \sin\theta \cos\varphi \right) \right]^2 \right. \\ &\quad + \left[\frac{9}{8} \sin\left(\frac{k_{\max}\Delta}{2} \sin\theta \sin\varphi \right) - \frac{1}{24} \sin\left(\frac{3k_{\max}\Delta}{2} \sin\theta \sin\varphi \right) \right]^2 \\ &\quad \left. + \left[\frac{9}{8} \sin\left(\frac{k_{\max}\Delta}{2} \cos\theta \right) - \frac{1}{24} \sin\left(\frac{3k_{\max}\Delta}{2} \cos\theta \right) \right]^2 \right. \end{aligned} \tag{9}$$

Fig. 1 shows the value of $Q(\theta, \phi)$ varies with $\theta\theta$ and ϕ at the fixed parameter $k_{\max}\Delta = 0.1\pi$. The maximum value of the function $Q(\theta, \phi)$ is obtained at $\theta = arcos\sqrt{1/3} \approx 0.304\pi$, $\varphi = 0.25\pi$. Note that the calculation results reveal that the maximum values of $Q(\theta, \phi)$ located at the same point ($\theta = 0.304\pi$, $\varphi = 0.25\pi$) for different values of $k_{\max}\Delta$. Thus, by substituting $\theta = 0.304\pi$ and $\varphi = 0.25\pi$ into (9), we can get the maximum value $Q_{\max}(0.304\pi, 0.25\pi)$, and then according to (6), the condition for Δt_{SF} is derived as

$$\begin{aligned} \Delta t_{\mathrm{SF}} &\le \frac{\Delta}{c_0} \times \frac{3.003}{2} \times \frac{1}{\sqrt{\mathrm{Q}_{\max}}} = 0.7431 \times \frac{\Delta}{c_0} \times \mathrm{CE} \\ &= \Delta t_{\mathrm{CFL}} \times \mathrm{CE} \end{aligned} \tag{10}$$

where Δt_{CFL} is the CFL limitation of the 3-D standard SFDTD$^{(4,4)}$ method and CE denotes the extended factor and is expressed as

$$\mathrm{CE} = 2.206/\sqrt{\mathrm{Q}_{\max}(k_{\max}\Delta)}. \tag{11}$$

As shown in Fig. 2, the values of CE are greater than 1 for the $k_{\max}\Delta$ from 0 to π. Therefore, the upper limit of the Δt_{SF} in (10) is greater than that of the Δt_{CFL} in (7).

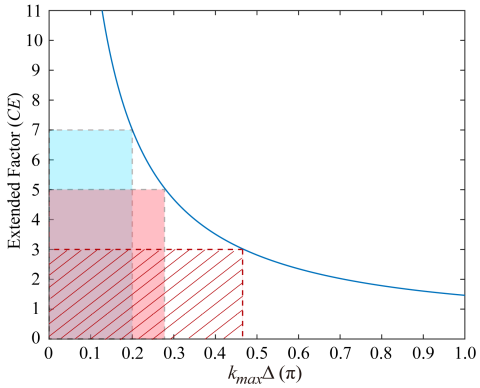

Fig. 2. Value of CE varying with $k_{\max}\Delta$.

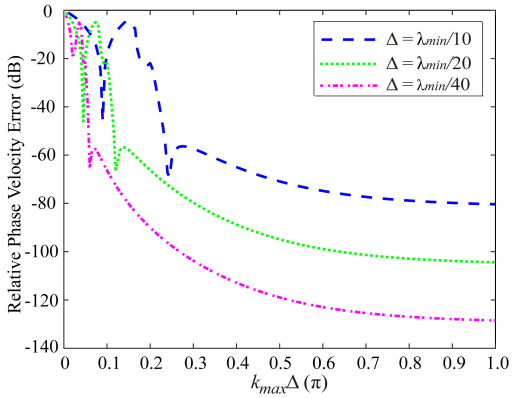

Fig. 3. Value of relative phase velocity errors E_{rr} in (14) for $\Delta = \lambda_{\min}/10$, $\Delta = \lambda_{\min}/20$, and $\Delta = \lambda_{\min}/40$.

B. Numerical Dispersion Analysis of SF-SFDTD$^{(4,4)}$ Method

The variation between numerical propagation velocity and physical propagation velocity is a significant indicator for determining the numerical dispersion property of the numerical method. The numerical dispersion equation of the standard SFDTD$^{(4,4)}$ method is written as

$$\omega\Delta t = \arccos\left(1 + \frac{1}{2}\sum_{l=1}^{m} g_l \left\{c_0^2\Delta t^2\left(\eta_x^2 + \eta_y^2 + \eta_z^2\right)\right\}^l\right). \quad (12)$$

After substituting the extended time stability condition of Δt_{SF} in (10) into the dispersion relation of standard SFDTD$^{(4,4)}$ method [see (12)], for the wave propagating along the angles of $\theta = 0.304\pi$, $\phi = 0.304\pi$, thus the numerical phase velocity of the proposed 3-D highly stable SF-SFDTD$^{(4,4)}$ method can be derived as

$$\omega = \frac{1}{\Delta t_{\text{CFL}} \times \text{CE}\left(k_{\max}\Delta\right)} \times \arccos\left(1 + \frac{1}{2}\sum_{l=1}^{m} g_l \left\{c_0^2\left(\Delta t_{\text{CFL}} \times \text{CE}\left(k_{\max}\Delta\right)\right)^2 \times \text{Q}\left(k_p, 0.304\pi, 0.25\pi\right)/\Delta^2\right\}^l\right) \quad (13)$$

It should be noted that the numerical wavenumber $k_{\max}$ in (9) is chosen as k_p, then, the relative numerical phase velocity error is defined as

$$E_n = 20\log\left(\left|v_p - v_0\right|/\left|v_0\right|\right) \quad (14)$$

and $v_p = \omega/k_p$ is the numerical phase velocity.

Fig. 3 shows that the relative phase velocity errors (E_{rr}) of the SF-SFDTD$^{(4,4)}$ method vary with $k_{\max}\Delta$.According to the results of Figs. 2 and 3, it can be concluded that the relative phase velocity error reduces when Δ decreases.

C. Application of SF-SFDTD$^{(4,4)}$ Method in Subgrid Scheme

In this study, a novel subgrid technique is proposed by combining the standard FDTD$^{(2,2)}$ method and the SF-SFDTD$^{(4,4)}$ method is presented. The field components within the coarse grid region are updated through the implementation of the standard FDTD$^{(2,2)}$ method, while the SF-SFDTD$^{(4,4)}$ method is applied to the dense grid region. This approach allows for the relaxation of the time step beyond the CFL limitation. Due to the extended stability of the SF-SFDTD$^{(4,4)}$ method, a larger time step that satisfies the coarse grid CFL condition can be chosen for the dense grid region. One advantage of this technique is that it eliminates the need for temporal domain interpolation, as the interpolation scheme only needs to be implemented in the spatial domain. In a 3-D subgrid scheme, there are six interfaces between the coarse and dense grid regions. For the sake of simplicity, we will focus on the spatial interpolation procedures for one interface. As shown in Fig. 4, the dense grid e_x values on the interface are unknown and cannot be obtained using the SF-SFDTD$^{(4,4)}$ method. Therefore, to determine the dense grid e_x value on the interface, spatial interpolation can be performed within the coarse-grid domain on the interface.

Fig. 5(a) illustrates the distribution diagram of e_x (E_x) on the interface between the coarse and dense grids for $j_F = j_A$ ($j_f = 1$) as shown in Fig. 4. The subscript F denotes the coordinate in the coarse-grid region while the subscript f denotes the coordinate in the dense-grid region. Within the dense-grid domain, the value $e_x(i_f + 1/2 + m_1, 1, k_f + m_2)$ can be obtained using the following spatial interpolation expression.

Case 1: $m_1 \le M/2$.

$$\begin{aligned} e_x\left(i_f + \frac{1}{2} + m_1, 1, k_f + m_2\right) &= \frac{(M + 2m_1 - 1)(M - m_2 + 1)}{2M^2} E_x^n\left(i_F + \frac{1}{2}, j_A, k_F\right) \\ &+ \frac{(M - 2m_1 + 1)(M - m_2 + 1)}{2M^2} E_x^n\left(i_F - \frac{1}{2}, j_A, k_F\right) \\ &+ \frac{(M + 2m_1 - 1)(m_2 - 1)}{2M^2} E_x^n\left(i_F + \frac{1}{2}, j_A, k_F + 1\right) \\ &+ \frac{(M - 2m_1 + 1)(m_2 - 1)}{2M^2} E_x^n\left(i_F - \frac{1}{2}, j_A, k_F + 1\right) \end{aligned} \quad (15)$$

Case 2: $M/2 < m_1 \le M$

$$\begin{aligned} e_x\left(i_f + \frac{1}{2} + m_1, 1, k_f + m_2\right) &= \frac{(3M - 2m_1 + 1)(M - m_2 + 1)}{2M^2} E_x^n\left(i_F + \frac{1}{2}, j_A, k_F\right) \\ &+ \frac{(2m_1 - M - 1)(M - m_2 + 1)}{2M^2} E_x^n\left(i_F + \frac{3}{2}, j_A, k_F\right) \\ &+ \frac{(3M - 2m_1 + 1)(m_2 - 1)}{2M^2} E_x^n\left(i_F + \frac{1}{2}, j_A, k_F + 1\right) \\ &+ \frac{(2m_1 - M - 1)(m_2 - 1)}{2M^2} E_x^n\left(i_F + \frac{3}{2}, j_A, k_F + 1\right) \end{aligned} \quad (16)$$

where m_1 and m_2 represent both integers, $1 \le m_1, m_2 \le M$, M denotes size ratio between coarse and dense grid. I_F and k_F on the interface denote grid coordinates of the coarse grid in the x- and z-directions ($i_A \le i_F \le i_B$, $k_A \le k_F \le k_B$), respectively. Similarly, $i_f + m_1$ and $k_f + m_2$ on the interface denote grid coordinates of the dense grid in the x- and z-directions ($i_f = M\times(i_F - i_A)$, $k_f = M\times(k_F - k_A)$), respectively. (i_A, i_B), (j_A, j_B), and (k_A, k_B), refer to the front and rear interface along x-, y-, and z-directions, respectively.

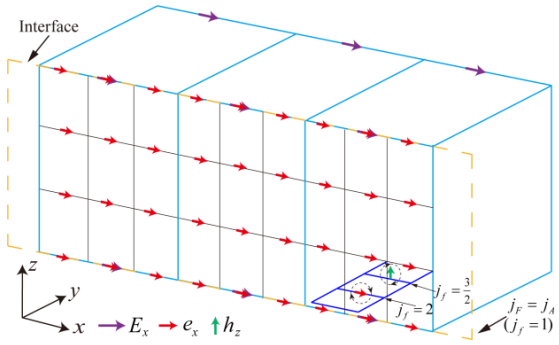

Fig. 4. Interface between coarse and dense grid regions.

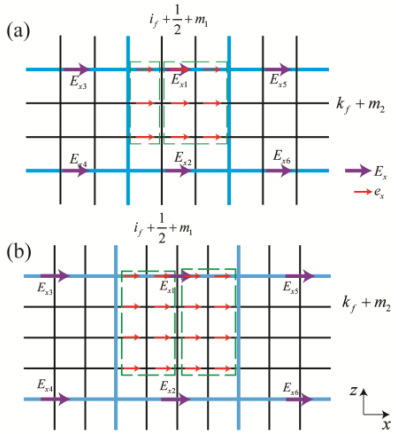

Fig. 5. Interpolation diagram of e_x on the interface. (a) Odd ratio. (b) Even ratio.

In Fig. 5(a), e_x in the box on the left belongs to case 1, and e_x is calculated by (15). While ones in the box on the right belong to case 2, (16) is employed to carry out the interpolation, therefore, we could obtain $E_{x1} = E_x(i_F + 1/2, j_A, k_F)$, $E_{x2} = E_x(i_F + 1/2, j_A, k_F + 1)$, $E_{x3} = E_x(i_F - 1/2, j_A, k_F)$, $E_{x3} = E_x(i_F - 1/2, j_A, k_F)$, $E_{x4} = E_x(i_F - 1/2, j_A, k_F + 1)$, $E_{x5} = E_x(i_F + 3/2, j_A, k_F)$, and $E_{x6} = E_x(i_F + 3/2, j_A, k_F + 1)$. The spatial interpolation method described above, which corresponds to an odd ratio between the coarse and dense grids, is also applicable for the even ratio, as depicted in Fig. 5(b). It is noted that SF-SFDTD$^{(4,4)}$ method is used in the dense grid region, i.e., a 4th-order finite difference scheme is utilized to discretize the 1st-order partial derivative in space

$$\left(\frac{\partial F^n}{\partial \delta}\right) = \alpha_1 \times \left[F^n\left(h + \frac{1}{2}\right) - F^n\left(h - \frac{1}{2}\right)\right] \Big/ \Delta\delta - \alpha_2 \times \left[F^n\left(h + \frac{3}{2}\right) - F^n\left(h - \frac{3}{2}\right)\right] \Big/ \Delta\delta. \quad (17)$$

where F denotes the EM fields, $\delta = (x, y, z)$, and α_1 and α_1 represent the difference coefficients. According to (17), all the dense grid electric fields **e** (magnetic fields **h**) should be calculated by the surrounding eight magnetic fields **h** (electric fields **e**). However, taking the field e_x, located one dense grid away from the interface as an example (illustration in the lower right corner of Fig. 3, $j_f = 2$), some magnetic fields **h** are missing if (17) is used to update the field e_x, the same problem occurs when calculating the magnetic field h_z, located at half of a dense grid away from the interface (illustration in the lower right corner of Fig. 3, $j_f = 3/2$). To solve this problem, the SF-SFDTD$^{(4,2)}$ method is adopted. The method has 2nd-order accuracy in the spatial domain to calculate these dense grid EM fields. Next, the rest of the EM field in dense grid region are updated with the SF-SFDTD$^{(4,4)}$ method.

Following the update of the EM fields in the dense grid region, the EM fields on the coarse grid located within the dense grid region require interpolation and modification. This is achieved by employing the subsequent equations (The x-direction is used as an example and the interpolation modification formula remains consistent across other directions).

If M is the odd

$$E_x^{n+1/2}\left(i_F + \frac{1}{2}, j_F, k_F\right) = e_x^{n+1/2}\left(i_f + \frac{M}{2}, j_f + 1, k_f + 1\right) \quad (18)$$

$$H_x^{n+1}\left(i_F, j_F + \frac{1}{2}, k_F + \frac{1}{2}\right) = h_x^{n+1}\left(i_f + 1, j_f + \frac{M}{2}, k_f + \frac{M}{2}\right) \quad (19)$$

If M is the even, (20) and (21), as shown at the bottom of the page.

In summary, the calculation steps of the proposed hybrid subgrid technique are described as follows:

1) The coarse grid **E** and **H** fields are calculated with the standard FDTD$^{(2,2)}$ method.

2) The dense grid **e** fields on the interface of the coarse and dense grid region are calculated through (15) and (16).

3) The dense grid fields **e**, located one of a dense grid away from the interface, and the dense grid fields **h**, located half of a dense grid away from the interface, are calculated utilizing the SF-SFDTD$^{(4,2)}$ method.

4) The remaining dense grid **e** and **h** fields inside the dense grid region are calculated using the SF-SFDTD$^{(4,4)}$ method.

5) The coarse grid **E** and **H** located at the dense grid region are modified by (18) and (19) for odd ratio, or (20) and (21) for even ratio.

III. Numerical Results

A. 3-D Resonance Cavity Model

The efficiency and correctness of the proposed SF-SFDTD$^{(4,4)}$ method are confirmed using a 3-D metallic resonance cavity model. The length of the cavity in each direction is set as 1 m, and a soft Gaussian pulse with the expression of $e^{-[(t-t_0)/T_s]^2}$, ($T_s = 1.0618$ ns and $t_0 = 4\ T_s$) is adopted. The spatial size of the cubic grid is $\Delta = 0.05/3$ m, and Δt is set to be 0.99 times of Δt_{CFL} [see (7)] in standard SFDTD$^{(4,4)}$ method. For the SF-SFDTD$^{(4,4)}$ method, $\Delta t_{\mathrm{SF}} = 3\Delta t, 5\Delta t, 7\Delta t$ (CE = 2.97, 4.95, and 6.93) are considered. Fig. 6 displays the resonant modes of the 3-D cavity, calculated by both the standard SFDTD$^{(4,4)}$ method (i.e., CE = 0.99) and the SF-SFDTD$^{(4,4)}$ approach (CE = 2.97, 4.95, and 6.93). The results obtained by the SF-SFDTD$^{(4,4)}$ method with different time steps (Δt_{SF}) are consistent of SFDTD$^{(4,4)}$ method. Finally, the execution time of SFDTD$^{(4,4)}$ method and SF-SFDTD$^{(4,4)}$ method are listed in Table I. The execution time of SF-SFDTD$^{(4,4)}$ method is almost

$$E_x^{n+1/2}\left(i_F + \frac{1}{2}, j_F, k_F\right) = \frac{1}{2}\left[\begin{array}{l} e_x^{n+1/2}\left(i_f + \frac{1}{2} + \frac{M}{2}, j_f + 1, k_f + 1\right) \\ + e_x^{n+1/2}\left(i_f + \frac{1}{2} + \frac{M}{2} + 1, j_f + 1, k_f + 1\right) \end{array}\right] \quad (20)$$

$$H_x^{n+1}\left(i_F, j_F + \frac{1}{2}, k_F + \frac{1}{2}\right) = \frac{1}{4} \times \left[\begin{array}{l} h_x^{n+1}\left(i_f + 1, j_f + \frac{M+1}{2}, k_f + \frac{M+1}{2}\right) + h_x^{n+1}\left(i_f + 1, j_f + \frac{M+3}{2}, k_f + \frac{M+1}{2}\right) \\ + h_x^{n+1}\left(i_f + 1, j_f + \frac{M+1}{2}, k_f + \frac{M+3}{2}\right) + h_x^{n+1}\left(i_f + 1, j_f + \frac{M+3}{2}, k_f + \frac{M+3}{2}\right) \end{array}\right] \quad (21)$$

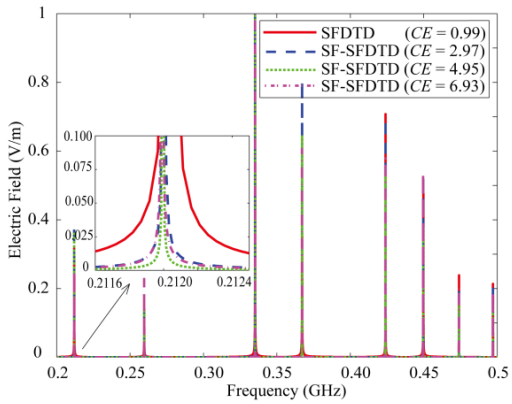

Fig. 6. Resonant frequencies of a 3-D cavity obtained by different methods.

TABLE I

EXECUTION TIME (S) FOR SFDTD$^{(4,4)}$ AND SF-SFDTD$^{(4,4)}$ METHODS (INTEL(R) CORE[1] I7-10700K CPU AT 3.79 GHz)

Method	*CE*	Time steps	Execution time (s)
SFDTD$^{(4,4)}$	0.99	10500	1326.32
SF-SFDTD$^{(4,4)}$	2.97	3500	1379.79
SF-SFDTD$^{(4,4)}$	4.95	2100	829.43
SF-SFDTD$^{(4,4)}$	6.93	1500	594.16

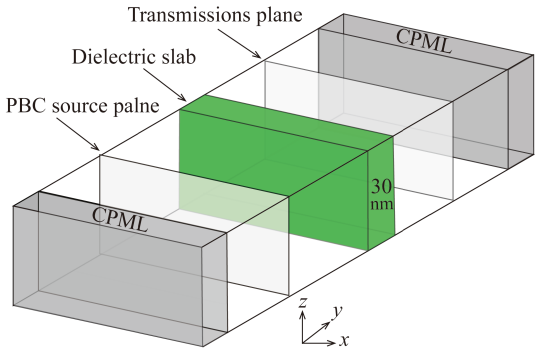

Fig. 7. Simulation configurations of the 3-D rectangular waveguide.

identical as that of the standard SFDTD$^{(4,4)}$ method when CE = 2.97, revealing that the efficiency of the SF-SFDTD$^{(4,4)}$ method surpasses the SFDTD$^{(4,4)}$ method when CE is larger than 2.97.

B. Reflection Coefficient of Dielectric Slab

To further verify the accuracy of the SF-SFDTD$^{(4,4)}$ method, a study on the reflectivity characteristics of a dielectric slab was conducted. A 3-D model of a rectangular waveguide containing a dielectric slab ($\varepsilon_r = 16\varepsilon_r = 16$) was considered for this purpose. The dielectric slab, with a thickness of 30 nm, was positioned at the center of the rectangular waveguide. Additionally, the convolutional perfectly matched layer (CPML) was applied at both ends of the simulation domain. Fig. 7 illustrates the configuration of the slab within the waveguide, where a plane wave with a Gaussian pulse propagates along the y-direction. The Gaussian function parameters were set as $T_s = 0.1062$ fs, $t_0 = 4\ T_s$. The grid size was selected as 0.2 nm. It is worth noting that the CFL limitation of the conventional SFDTD$^{(4,4)}$ algorithm is influenced by the grid size along the direction of the propagating wave. Hence, the upper-limit temporal increment (Δt_{CFL}) in the standard SFDTD$^{(4,4)}$ method is 1.287(d y/c_0).

Fig. 8 presents the reflection coefficients obtained using the SFDTD$^{(4,4)}$ method (CE = 0.99) and the SF-SFDTD$^{(4,4)}$ method

[1]Trademarked.

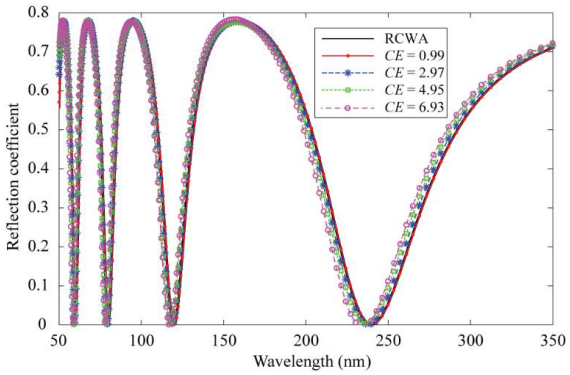

Fig. 8. Reflection coefficient calculated by the RCWA, SFDTD, and SF-SFDTD method.

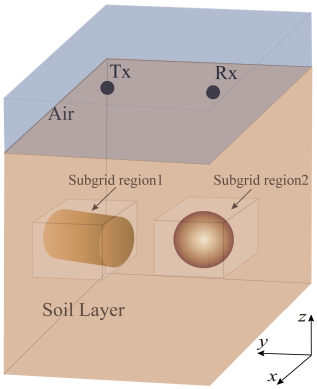

Fig. 9. Classical 3-D GPR system model, dielectric sphere as a detection target.

(CE = 2.97, 4.95, and 6.93). The rigorous coupled wave analysis (RCWA) method is employed as a benchmark for comparison. The results obtained by the SF-SFDTD$^{(4,4)}$ method demonstrate agreement with both the analytical results and the standard SFDTD$^{(4,4)}$ method. This finding confirms the efficacy of the SF-SFDTD$^{(4,4)}$ method as an efficient technique for EM model simulation. It is worth noting that the calculation error between the analytical and numerical methods increases as the time step increases. This is attributed to the larger numerical dispersion error of the SF-SFDTD$^{(4,4)}$ method with increasing time step. In addition, the presence of inhomogeneous permittivity within the calculation domain can also impact the computational accuracy of the SF-SFDTD$^{(4,4)}$ method.

C. Subgrid Technique for Simulating GPR Scene

Additionally, to further verify the benefits of the proposed hybrid subgrid technique, a simulation of a classical ground penetrating radar (GPR) scene is conducted, as depicted in Fig. 9. In this scenario, the transmitting antenna serves as the excitation source point in free space, while the receiving antenna functions as the probe point for receiving detection signals. The expression of the source is presented

$$\mathrm{pulse}(t) = \begin{cases} -(2\pi/\tau)\sum_{n=1}^{3} a_n n \sin(2\pi n t/\tau), & 0 < t < \tau \\ 0, & \text{other} \end{cases} \tag{22}$$

where the center frequency is 200 MHz, the relaxation time $\tau = 1.55/f_c$, coefficients $a_1 = -0.488$, $a_2 = 0.145$, and $a_3 = -0.0102$.

The simulated half-space model comprises an air layer and a soil layer, with the frequency-dependent property of the soil described using the multipole Debye model. To absorb EM waves, the CPML is employed [9], [10]. The parameters for the soil's multipole Debye

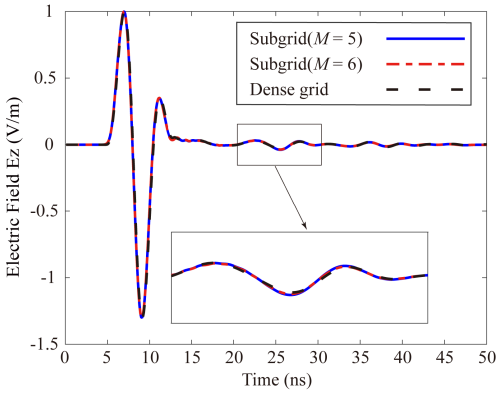

Fig. 10. Time-domain results of Ez at the receiving antenna.

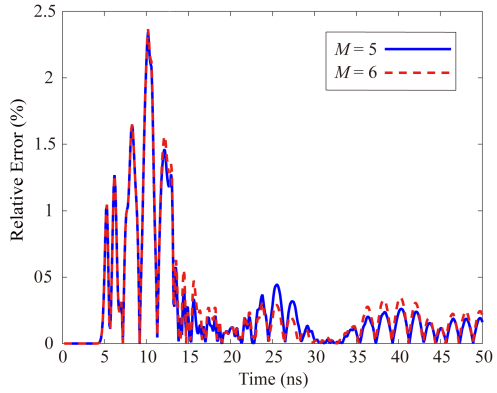

Fig. 11. Relative calculation error of the hybrid subgrid SF-SFDTD$^{(4,4)}$ method with different ratios.

model are as follows: $\varepsilon_\infty = 3.2$, $\tau_1 = 2.71$ ns, $\Delta\varepsilon_1 = 0.75$, $\tau_2 = 0.108$ ns, and $\Delta\varepsilon_2 = 0.3$, and conductivity $\sigma = 0.397 \times 10^{-3}$ S/m. The dimensions of the entire simulation domain are $4.8 \times 4.8 \times 4.8$ m, with a coarse grid size of $\Delta x = \Delta y = \Delta z = 0.06$ m. Both the transmitting and receiving antennas are positioned 0.3 m above the soil surface, and the distance between them (Tx–Rx) is 1.5 m. The two detection targets, a dielectric sphere and a dielectric cylinder, are situated within the same soil layer. The dielectric sphere has a relative permittivity of is 10 and a radius of 0.24 m. The dielectric cylinder has a relative permittivity of 20, a radius of 0.18 m, and a length of 0.48 m in the y direction. The centers of the sphere and cylinder are located 0.6 m below the soil, with a separation of 1.2 m in the y direction. Additionally, each subgrid region has dimensions of $0.6 \times 0.6 \times 0.6$ m. For comparison purposes, purposes, the standard FDTD$^{(2,2)}$ method employs a uniform dense grid ($\Delta x_f = \Delta y_f = \Delta z_f = 0.02$ m) as a reference for numerical results. Moreover, to assess the versatility of the subgrid technology in refining the coarse grid with odd and even ratios, different ratios between the coarse and dense grid sizes are implemented in the proposed subgrid technique. Fig. 10 illustrates the time-domain waveforms at the receiving antenna, which are calculated using two hybrid subgrid SF-SFDTD methods with coarse- and dense-grid ratios of 1:5 and 1:6, respectively, as well as the dense grid FDTD$^{(2,2)}$ method. Subsequently, the quantified numerical error of the proposed method, in comparison to the dense grid FDTD$^{(2,2)}$ method is calculated using the following equation:

$$E_r = \frac{\left|E_{z\_\text{danso}} - E_{z\_\text{subgid}}\right|}{\max\left|E_{z\_\text{dansos}}\right|} \times 100\%. \tag{23}$$

Evidently, the small relative errors of the hybrid subgrid SF-SFDTD$^{(4,4)}$ methods with ratios of 1:5 and 1:6 can be observed in Fig. 11. These results provide compelling evidence for the accuracy of the hybrid subgrid method in simulating the GPR scene. Additionally, this method can realize odd and even times meshes for the coarse grid. Moreover, Table II presents an analysis of the memory cost and CPU time for various approaches. A comparison with the conventional dense grid FDTD$^{(2,2)}$ method reveals that the proposed subgrid SF-SFDTD$^{(4,4)}$ method offers significant computational advantages in simulating the GPR scene.

TABLE II

MEMORY COST (MB) AND EXECUTION TIME (S) FOR FDTD$^{(2,2)}$ AND HYBRID SUBGRID METHODS (INTEL(R) CORE[1] I7-10700K CPU AT 3.79 GHZ)

Method	Memory Cost (MB)	Execution Time (s)
Dense grid FDTD$^{(2,2)}$	472.08	2759.15
Subgrid SF-SFDTD$^{(4,4)}$ ($M = 5$)	107.03	264.31
Subgrid SF-SFDTD$^{(4,4)}$ ($M = 6$)	196.25	552.54

IV. CONCLUSION

In this communication, an efficient and highly stable algorithm, namely, SF-SFDTD$^{(4,4)}$, is introduced. Theoretical analysis reveals that the stability condition of the conventional SFDTD$^{(4,4)}$ algorithm can be extended beyond the CFL limitation by eliminating unstable components in the spatial frequency domain. The SF method, in comparison to implicit numerical approaches, effectively extends the CFL limitation without the need for complex formula derivation and matrix operations. To confirm the advantages of the proposed algorithm over the standard SFDTD$^{(4,4)}$ method, a numerical example analysis is carried out. Additionally, the application of the SF-SFDTD$^{(4,4)}$ method to the hybrid 3-D subgrid scheme is presented. This hybrid subgrid technique allows for the generation of coarse and dense grids in arbitrary ratios, showcasing its versatility. The hybrid subgrid method exhibits significant advantages in terms of efficiency and memory cost.

REFERENCES

[1] K. Yee, "Numerical solution of initial boundary value problems involving Maxwell's equations in isotropic media," *IEEE Trans. Antennas Propag.*, vol. AP-14, no. 3, pp. 302–307, May 1966.

[2] A. Taflove and S. C. Hagness, *Computational Electrodynamics the Finite Difference Time-Domain Method*, 3rd ed. Boston, MA, USA: Artech House, 2005.

[3] J. Fang, "Time domain finite difference computation for Maxwell's equations," Ph.D. dissertation, Dept. Elect. Eng., Univ. California Berkeley, Berkeley, CA, USA, 1989.

[4] T. Hirono, W. Lui, S. Seki, and Y. Yoshikuni, "A three-dimensional fourth-order finite-difference time-domain scheme using a symplectic integrator propagator," *IEEE Trans. Microw. Theory Tech.*, vol. 49, no. 9, pp. 1640–1648, Sep. 2001.

[5] W. Sha, Z. Huang, M. Chen, and X. Wu, "Survey on symplectic finite-difference time-domain schemes for Maxwell's equations," *IEEE Trans. Antennas Propag.*, vol. 56, no. 2, pp. 493–500, Feb. 2008.

[6] C. D. Sarris, "Extending the stability limit of the FDTD method with spatial filtering," *IEEE Microw. Wireless Compon. Lett.*, vol. 21, no. 4, pp. 176–178, Apr. 2011.

[7] C. Chang and C. D. Sarris, "A spatially filtered finite-difference time-domain scheme with controllable stability beyond the CFL limit: Theory and applications," *IEEE Trans. Microw. Theory Techn.*, vol. 61, no. 1, pp. 351–359, Jan. 2013.

[8] Z. Y. Long, "Introduction of the Debye media to the filtered finite-difference time-domain method with complex-frequency-shifted perfectly matched layer absorbing boundary conditions," Ph.D. thesis, Dept. Elect. Electron. Eng., Univ. Manchester, Manchester, U.K., 2017.

[9] J. A. Roden and S. D. Gedney, "Convolution PML (CPML): An efficient FDTD implementation of the CFS-PML for arbitrary media," *Microw. Opt. Technol. Lett.*, vol. 27, no. 5, pp. 334–339, Dec. 2000.

[10] J. Li and J. Dai, "Z-transform implementations of the CFS-PML," *IEEE Antennas Wireless Propag. Lett.*, vol. 5, pp. 410–413, 2006.